

Contents lists available at ScienceDirect

Aerospace Science and Technology

www.elsevier.com/locate/aescte



Aerodynamic shape optimization using a time spectral coupled adjoint for nonlinear aeroelastic problems



Rachit Prasad^a, Seongim Choi^{b,*}, Mayuresh Patil^a

- ^a Virginia Polytechnic Institute and State University, Blacksburg, VA, 24060, United States of America
- b School of Mechanical Engineering, Gwangju Institute of Science Technology (GIST), 123 Cheomdangwagi-ro, Buk-gu, Gwangju, 61005, South Korea

ARTICLE INFO

Article history: Received 20 October 2020 Received in revised form 27 January 2022 Accepted 9 March 2022 Available online 15 March 2022 Communicated by Z. Weiwei

ABSTRACT

In this work, prediction of flutter and Limit Cycle Oscillations (LCO) for the aircraft wing has been carried out using a coupled, time spectral computational fluid dynamics (CFD) and computational structural dynamics (CSD) method. Flutter related shape design has also been carried out using a coupled, adjoint based sensitivity analysis framework. A discrete adjoint solver was developed in time-spectral form to calculate coupled sensitivity of the dynamic aeroelastic motion. The total structural energy was constrained at different levels to determine the flutter onset conditions or different LCO solutions. Compared to the time-marching approach, the time-spectral method not only enables faster convergence for unsteady problems, but also leads to significant improvement in implementation of adjoint based sensitivity analysis. Unlike the time-marching approach, there is no high memory requirement for time-spectral approach. The proposed method was applied to a pitch-plunge airfoil section at transonic flight conditions. The flutter and LCO results showed great agreements with time-marching results. The adjoint based sensitivity values were validated by finite difference based results, showing great agreement with errors less than 2%. Finally, aerodynamic shape optimization was carried out with the design objective of maximizing the flutter velocity, with and without constraint on the drag coefficient, respectively. Significant increase in flutter boundary velocity was observed in both cases.

© 2022 Elsevier Masson SAS. All rights reserved.

Contents

1.	Introd	luction	2
2.	Aeroe	elastic modeling	3
	2.1.	Governing equations for aerodynamics	
	2.2.	Governing equations for structures	3
3.	Flutte	r/LCO prediction	4
	3.1.	Energy and phase constraints	4
	3.2.	Update equations for frequency and velocity	5
	3.3.	Fluid structure interaction and implementation	5
4.	Time-	spectral adjoint formulation for flutter and LCO problems	6
	4.1.	Derivation of the adjoint equations for sensitivity analysis	6
	4.2.	Jacobian sub-matrices of the adjoint equations	7
5.	Result	ts	8
	5.1.	Implementation and validation	
	5.2.	Prediction of flutter and LCO conditions	9
	5.3.	Adjoint sensitivity analysis	10
	5.4.	Computational cost and numerical stability	12
	5.5.	Shape optimization results	12
6	Concl	usion	15

E-mail address: schoi1@gist.ac.kr (S. Choi).

^{*} Corresponding author.

Declaration of competing interest	. 16
References	. 17

1. Introduction

The desire to have aircrafts with greater aerodynamic efficiency has led to aircraft designs with high aspect ratio wings, exhibiting high flexibility. With this trend, it has become increasingly important to include aeroelastic performance in the design process. While there are static aeroelastic effects such as divergence that needs to be considered, the main focus of this work is to look at wing design with emphasis on the dynamic aeroelastic phenomenon, which mainly includes flutter onset and LCOs. In order to carry out gradient based design optimization, it is important to compute flutter onset and LCO solutions and their gradients in a computationally accurate and efficient manner.

Comparing flutter and LCO, the former can be evaluated in an efficient manner by using linear aeroelastic methods, such as the p-k method. This approach works well for flow conditions where the flutter onset is primarily driven by linear aerodynamic effects, such as subsonic flow. However, the method fails to capture nonlinear flow features such as vortex shedding, separation, and turbulence, effects of which can lead to dynamic aeroelastic interactions (e.g. buffeting, LCOs, etc.). It is thus essential to couple nonlinear CFD and CSD methods to accurately model different kinds of LCOs and other nonlinear dynamic aeroelastic effects. The coupled nonlinear aeroelastic system can be solved using the time-accurate approach by marching the coupled fluid-structure solution in the time domain. A number of studies have successfully predicted both flutter and LCO characteristics in transonic flow regime using this approach. Lee-Rausch and Batina [1] and Liu et al. [2] coupled an Euler CFD solver with a modal truncation based reduced order structural model. Farhat [3] coupled an Euler CFD solver with a full linear FEM model to predict flutter characteristics. Bendiksen [4,5] was able to successfully predict LCOs in transonic flows, using the time-accurate approach. Djayapertapa and Allen [6,7] extensively studied transonic flutter by solving the Euler equations in time domain and developed control laws to suppress flutter through active flap control. Taylor et al. [8] extended Djayapertapa and Allen's work to three dimensional wing configurations. Allen et al. [9] proposed and developed a reduced order model to accurately capture the nonlinear physics of transonic flutter and be able to rapidly predict flutter conditions.

While aeroelastic problems can be solved in the time domain, for periodic problems, the solution procedure can be further sped up by solving the aeroelastic equations using the time-spectral method. The time-spectral method approximates the solution as a discrete Fourier series with finite number of harmonics. Although the computational cost is dependent on the number of harmonics in the approximation, it typically has a reduced computational cost compared to the time-accurate method. The method has been successfully applied to analyze periodic flows in turbomachinery [10,11], pitching airfoil [12], rotor flight [13] and open rotors [14].

Subsequently, the method was extended to solve periodic aeroelastic problems, including flutter and LCOs. Predicting LCOs using the time spectral method requires additional consideration as the method requires a priori knowledge of the LCO frequency, which is not known and hence must be computed as a part of the solution procedure. Thomas et al. [16] and Yao [19] developed their own time-spectral method based approaches to compute LCO solutions for airfoil in transonic flow. Ekici and Hall [15] used the method to predict LCO characteristics in turbomachinery.

Predicting the flutter onset condition using the time spectral method has additional complexity as compared to LCO prediction, as for the flutter problem, the flutter onset velocity also needs to be computed along with the flutter frequency. Liu et al. [17] developed a harmonic balance based method and compared their results with frequency domain based V-g method. Gong and Zhang [18] developed a time spectral based method, which uses a double iteration approach, to predict flutter and LCO characteristics.

In order to carry out gradient based design optimization, the adjoint based sensitivity analysis is popularly used in aerodynamic shape design [20–25]. Unlike traditional sensitivity analysis methods such as finite difference, the computational cost of calculating the gradient with respect to design variables is practically independent to the number of design variables. Hence, lot of design parameters can be optimized to achieve superior performance. Martins et al. [28]-[29] first carried out adjoint based sensitivity analysis for a steady, coupled aero-structural system for the purpose of design optimization. Maute et al. also carried out sensitivity analysis for a steady coupled aero-structural system, treating it as a three field system and used both the direct and adjoint [31] method.

However for unsteady problems, the adjoint based sensitivity analysis is difficult to apply as it requires the flow and adjoint variables to be stored at each time step [28]. This can be overcome for periodic problems by adopting the time-spectral method as it requires the solution to be stored at a few collocation points, and not every time step. This has been demonstrated by Huang and Ekici [26] and Rubino et al. [27]. Mani and Mavriplis [30] developed an unsteady adjoint based sensitivity analysis framework for an unsteady aero-structural system, solved using a time-accurate approach. Recently, similar approaches of carrying out adjoint based optimization of nonlinear aeroelastic systems have been carried out. Thomas and Dowell [32] have derived the adjoint based sensitivity analysis for their Fourier series approximation approach for the flutter/LCO prediction and carried out shape optimization. He et al. [33] have also developed their own time-spectral prediction based solver and adjoint sensitivity analysis for the flutter prediction and corresponding shape optimization. Chen et al. [34] employed the unsteady adjoint method improve the transonic fluid-structure interaction (FSI) stability by considering the aerodynamic damping coefficient as the objective function.

The contribution of the present work has been the development of a time spectral based method to compute the flutter and LCO solutions within the same framework. A corresponding framework for the adjoint based sensitivity analysis for flutter and LCO solutions has also been developed and its application to a shape design problem has been carried out. The impact of changes in airfoil shape on the flutter onset and LCO profile has been discussed in detail and can be further used in designing wings with delayed flutter onset characteristics.

The outline of the paper is as follows. The governing equations for the fluid and structures in their time-spectral form have been discussed in section 2. The proposed method of the flutter/LCO prediction is discussed in detail in section 3. This is followed by the adjoint based sensitivity analysis in section 4. Finally, the developed framework has been applied to a pitch plunge airfoil to predict the flutter and the coupled aeroelastic sensitivity is analyzed in Section 5 along with design optimization results.

Nome	Nomenclature						
$egin{array}{c} x_lpha \ \omega_h \ \omega_lpha \ r_lpha \ \mu \ U_\infty \ M \end{array}$	Static imbalance Plunge frequency Pitch frequency Non dimensionalized moment of inertia Mass ratio Freestream velocity Mass matrix of the structural model	r Freestr ω Freque E_{avg} Averag E_0 Fixed ϵ	ream Mach no. ream parameter ency of the TS method ge Total energy of the wing energy value				
K F _a u ù	Stiffness matrix of the structural model Aerodynamic nodal force vector Nodal displacement vector Nodal velocity vector	ref referer	flutter boundary nce values used pectral form/result				

2. Aeroelastic modeling

2.1. Governing equations for aerodynamics

The aerodynamics in this study has been modeled by unsteady Euler equations in Arbitrary Lagrangian Eulerian form. The equations have been discretized using the Finite Volume Method and hence, the integral form of the governing equations has been considered, as shown in Eq. (1a).

$$\iiint\limits_{V} \frac{\partial \mathbf{w}}{\partial t} dV + \iint\limits_{S} \mathbf{F} \cdot d\mathbf{S} = 0 \tag{1a}$$

$$\mathbf{w} = \begin{bmatrix} \rho \\ \rho \mathbf{v} \\ \rho E \end{bmatrix} \mathbf{F} = \begin{bmatrix} \rho(\mathbf{v} - \mathbf{v}_{\mathbf{x}}) \\ \rho \mathbf{v} \otimes (\mathbf{v} - \mathbf{v}_{\mathbf{x}}) + \bar{\mathbf{I}} p \\ \rho E(\mathbf{v} - \mathbf{v}_{\mathbf{x}}) + p \mathbf{v} \end{bmatrix}$$
(1b)

In Eq. (1b), ρ is the fluid density, \mathbf{v} is the fluid velocity, $\mathbf{v}_{\mathbf{x}}$ is the mesh velocity, E is the fluid internal energy and P is the fluid pressure. As the time-spectral method is used for temporal discretization, the state variables are approximated by a discrete Fourier series and the unsteady compressible inviscid equations in the time domain, described by Eq. (1a), are transformed to the frequency domain. However, solving for the solution in the frequency domain has its own challenges, such as representing the boundary conditions in the frequency domain. Instead, the frequency domain equations are then transposed back to the time domain using $2N_H + 1$ number of time instances, or collocation points, and the Fourier coefficients are solved for in the time domain. Detailed explanation for this can be found here [35]. The final form of the equation derived for the time-spectral method is given by Eq. (2). The fundamental frequency ω is used to expand the Fourier series.

$$\omega \mathbf{D} \mathbf{w}_{TS} V_{TS} + \mathbf{R}_{TS} (\mathbf{w}_{TS}) = 0 , \tag{2}$$

where $\vec{w_{TS}}$ and $\vec{R_{TS}}$ represent vectors of flow variables and residuals at collocation points, respectively. V_{TS} is the cell volume at the different time instances.

$$\mathbf{w_{TS}} = \begin{bmatrix} \mathbf{w}(t + \Delta t) \\ \mathbf{w}(t + 2\Delta t) \\ \vdots \\ \mathbf{w}(t + T) \end{bmatrix} \mathbf{R_{TS}} = \begin{bmatrix} \mathbf{R}(t + \Delta t) \\ \mathbf{R}(t + 2\Delta t) \\ \vdots \\ \mathbf{R}(t + T) \end{bmatrix}$$

As seen from Eq. (2), the unsteady term in the Euler equation is replaced by a matrix-vector product, where the spectral derivative matrix is defined as

$$D_{ij} = \begin{cases} 0, & i = j \\ \frac{1}{2} (-1)^{(i-j)} csc\left(\frac{(i-j)\pi}{2N_H - 1}\right), & i \neq j \end{cases}$$
 (3)

Eq. (2) can be rewritten as Eq. (4) with the addition of the pseudo time derivative term for solution convergence.

$$\frac{\partial \mathbf{w_{TS}}}{\partial \tau} + \omega D \mathbf{w_{TS}} V_{TS} + \mathbf{R_{TS}}(\mathbf{w_{TS}}) = 0 \tag{4}$$

2.2. Governing equations for structures

The structure has been modeled using the pitch/plunge typical airfoil configuration, the non-dimensional form of which is given by Eq (5).

Table 1 Structural parameters used in the airfoil section model.

Structural parameter	Value
x_{α}	0.25
r_{α}	$\sqrt{0.75}$
$\left(\frac{\omega_h}{\omega_{lpha}}\right)$	0.5
μ	75.0
ω_{lpha}	1.0 rad/s

$$\mathbf{M} \frac{d^{2}\mathbf{u}}{dt^{2}} + \mathbf{K}\mathbf{u} = \frac{4V^{2}\omega_{\alpha}^{2}}{\pi\mu} \mathbf{f}_{a}$$
where
$$\mathbf{M} = \begin{bmatrix} 1 & x_{\alpha} \\ x_{\alpha} & r_{\alpha}^{2} \end{bmatrix} \quad \mathbf{K} = \omega_{\alpha}^{2} \begin{bmatrix} \left(\frac{\omega_{h}}{\omega_{\alpha}}\right)^{2} & 0 \\ 0 & r_{\alpha}^{2} \end{bmatrix} \quad \mathbf{u} = \begin{cases} \frac{h}{b} \\ \alpha \end{cases} \quad \mathbf{f}_{a} = \begin{cases} -C_{l} \\ 2C_{m} \end{cases} \quad V = \frac{U_{\infty}}{c\omega_{\alpha}}$$
(5)

The structural parameters used in the above equation are given in Table 1. The chosen parameter values chosen result in prominent LCO behavior and has been used in other works in literature [11]. The damping has been assumed to be negligible and its effects have

Since the governing equations are solved by the time-spectral method, the structural dynamics equations need to be represented in time-spectral form. Starting from the governing equations for linear structural dynamics, given by Eq. (5), they can be converted to the first order form as given by Eq. (6).

$$\frac{d\mathbf{y}}{dt} + A\mathbf{y} - B\mathbf{f} = 0$$
where $\mathbf{A} = \begin{bmatrix} \mathbf{0} & -\mathbf{I} \\ \mathbf{M}^{-1}\mathbf{K} & \mathbf{0} \end{bmatrix}$ $\mathbf{B} = \begin{bmatrix} \mathbf{0} & \mathbf{0} \\ \mathbf{0} & \mathbf{M}^{-1} \end{bmatrix}$ $\mathbf{y} = \begin{bmatrix} \mathbf{u} \\ \dot{\mathbf{u}} \end{bmatrix}$ $\mathbf{f} = \begin{bmatrix} \mathbf{0} \\ \frac{4V^2 \omega_{\alpha}^2}{\pi \mu} \mathbf{f}_{\alpha} \end{bmatrix}$ (6)

Similarly to the aerodynamics governing equations, the unsteady term in Eq. (6) can be replaced by the matrix-vector product of spectral derivative term and structural state vector, as shown in Eq. (7). A pseudo time derivative term is added, as shown in Eq. (8), for convergence.

$$(\omega \mathbf{D} + \mathbf{A}) \mathbf{y}_{TS} - \mathbf{B} \mathbf{f}_{TS} = 0 \tag{7}$$

$$\frac{\partial \mathbf{y_{TS}}}{\partial \tau} + (\omega \mathbf{D} + \mathbf{A}) \mathbf{y_{TS}} - \mathbf{B} \mathbf{f_{TS}} = 0$$
(8)

where
$$\mathbf{y}_{TS} = \begin{bmatrix} \mathbf{y}(t + \Delta t) \\ \mathbf{y}(t + 2\Delta t) \\ \vdots \\ \mathbf{y}(t + T) \end{bmatrix}$$
 $\mathbf{f}_{TS} = \begin{bmatrix} \mathbf{f}(t + \Delta t) \\ \mathbf{f}(t + 2\Delta t) \\ \vdots \\ \mathbf{f}(t + T) \end{bmatrix}$

3. Flutter/LCO prediction

3.1. Energy and phase constraints

The periodic aero-structural solution at the flutter boundary is a non-unique solution and multiple periodic solutions can exist for the fluid and structural states with different amplitudes. Thus, in order to solve for a given state, an additional constraint needs to be imposed in the form of conserving the average structural energy over the period: $E_{avg}(y) - E_0 = 0$. The average energy of E_{avg} is calculated by integrating the total structural energy over a single time period, and given as

$$E_{avg} = \frac{1}{2\pi} \int_{0}^{2\pi} E(\theta) d\theta = \frac{1}{2\pi} \frac{1}{2} \int_{0}^{2\pi} \left(\mathbf{u}(\theta)^{T} \mathbf{K} \mathbf{u}(\theta) + \dot{\mathbf{u}}(\theta)^{T} \mathbf{M} \dot{\mathbf{u}}(\theta) \right) d\theta$$
(9)

where
$$\mathbf{u}(\theta) = \bar{\mathbf{u}}_0 + \sum_{n=1}^{N_H} (\bar{\mathbf{u}}_{sn} sin(\theta) + \bar{\mathbf{u}}_{cn} cos(\theta)), \dot{\mathbf{u}} = \bar{\dot{\mathbf{u}}}_0 + \sum_{n=1}^{N_H} (\bar{\dot{\mathbf{u}}}_{sn} sin(\theta) + \bar{\dot{\mathbf{u}}}_{cn} cos(\theta)).$$

The expression can then be simplified, leading to the expression given by Eq. (10). The average energy can then be expressed in terms of the solution state by the Fourier coefficients using the inverse Fourier Transform ($\bar{u} = Fu$).

$$E_{avg} = \frac{1}{2} \left(\bar{\boldsymbol{u}}_{0}^{T} \boldsymbol{K} \bar{\boldsymbol{u}}_{0} + \frac{1}{2} \sum_{n=1}^{N_{H}} \left(\bar{\boldsymbol{u}}_{sn}^{T} \boldsymbol{K} \bar{\boldsymbol{u}}_{sn} + \bar{\boldsymbol{u}}_{cn}^{T} \boldsymbol{K} \bar{\boldsymbol{u}}_{cn} \right) + \bar{\boldsymbol{u}}_{0}^{T} \boldsymbol{M} \bar{\boldsymbol{u}}_{0} + \frac{1}{2} \sum_{n=1}^{N_{H}} \left(\bar{\boldsymbol{u}}_{sn}^{T} \boldsymbol{M} \bar{\boldsymbol{u}}_{sn} + \bar{\boldsymbol{u}}_{cn}^{T} \boldsymbol{M} \bar{\boldsymbol{u}}_{cn} \right) \right)$$

$$(10)$$

This constraint is imposed by scaling the structural state variables by normalized total structural energy after the update of structures residual, that is $\mathbf{y} = \frac{\mathbf{y}}{\sqrt{e}}$, where $e = \frac{E_{avg}}{E_0}$.

Since the aero-structural system at the flutter boundary and LCOs are self-excited oscillations, the time-spectral solution is valid for any phase angle over its time period. Hence, a unique solution is obtained by fixing phase to an arbitrary value. This has been done by fixing one of the structural state variables to zero ($y_i = 0$). Having the energy and phase constraint closes the system of equations and leads to a unique solution. It should be noted that, by constraining the structural energy to be low enough, a periodic solution at the flutter boundary can be obtained. Different LCO velocities can be obtained at other higher energy levels. The proposed method works to obtain unique solutions at different energy levels.

3.2. Update equations for frequency and velocity

As observed from the governing equations, the time-spectral method requires the frequency of the problem to be known a priori, which is not known for self-excited phenomena like flutter and LCO. Additionally for the flutter boundary, the flutter velocity also needs to be known. For LCOs, different studies implemented different approaches to calculate the LCO frequency independently as a solution along with the fluid and structural states. One of the approaches, used by Ekici [15], involved updating the frequency, ω , by minimizing the L_2 norm of the structural residual, given by Eq. (11), with respect to ω and then solving for ω as shown in Eq. (12b). The idea behind this approach is that for the correct ω , the structural residual should be zero, and hence the desired ω should minimize the norm if the structural residual becomes close to zero.

$$L = \frac{1}{2} \mathbf{S}^T \mathbf{S} = \frac{1}{2} \left((\omega \mathbf{D} + \mathbf{A}) \mathbf{y_{TS}} - \mathbf{B} \mathbf{f_{TS}} \right)^T \left((\omega \mathbf{D} + \mathbf{A}) \mathbf{y_{TS}} - \mathbf{B} \mathbf{f_{TS}} \right)$$
(11)

$$\frac{\partial L}{\partial \omega} = \left(\frac{\partial \mathbf{S}}{\partial \omega}\right)^{T} \mathbf{S} = \left(\mathbf{D} \mathbf{y}_{TS}\right)^{T} \left(\left(\omega \mathbf{D} + \mathbf{A}\right) \mathbf{y}_{TS} - \mathbf{B} \mathbf{f}_{TS}\right) = 0 \tag{12a}$$

$$\omega^{n+1} = \frac{\left(\mathbf{D}\mathbf{y_{TS}}\right)^{T} \left(\mathbf{B}\mathbf{f_{TS}} - \mathbf{A}\mathbf{y_{TS}}\right)}{\left(\mathbf{D}\mathbf{y_{TS}}\right)^{T} \left(\mathbf{D}\mathbf{y_{TS}}\right)}$$
(12b)

However, the same approach cannot be applied to the computation of the flutter boundary, for which both the frequency and the velocity are unknown. In this study, rather than working with the velocity itself, the velocity is parameterized by a non-dimensional freestream pressure parameter, $r = \frac{p_{\infty}}{p_{ref}}$, which is freestream pressure, p_{∞} , normalized by reference pressure, p_{ref} . The freestream density has been assumed to be constant. With the assumption of the constant Mach number, freestream velocity, V_{∞} , can be written in terms of r, as shown in Eq. (13).

$$V_{\infty} = M_{\infty} \sqrt{\frac{\gamma p_{\infty}}{\rho_{\infty}}} = M_{\infty} \sqrt{\frac{\gamma r p_{ref}}{\rho_{ref}}} = M_{\infty} a_{ref} \sqrt{r}$$
(13)

An update scheme for r can be implemented to find the value at the flutter condition, r_F , which corresponds to the flutter speed, V_F . The velocity at the flutter boundary can also be computed by expanding the Ekici's approach to compute the LCO frequency [15]. Like for the LCO frequency, both the frequency and the velocity should minimize the structural residual at the flutter boundary. Two additional equations for ω and r can be written in Eq. (14a) and (14b), respectively, where the partial derivatives of the residual of the structural governing equations with respect to the frequency and the non-dimensional freestream pressure parameter are set to be zero. A fixed point iteration scheme can be used to solve for both ω and r, as shown in Eq. (15)

$$\frac{\partial L}{\partial \omega} = \left(\frac{\partial \mathbf{S}}{\partial \omega}\right)^{T} \mathbf{S} = \left(\mathbf{D} \mathbf{y}_{TS}\right)^{T} \left(\left(\omega \mathbf{D} + \mathbf{A}\right) \mathbf{y}_{TS} - r \mathbf{B} \bar{\mathbf{f}}_{TS}\right) = 0$$
(14a)

$$\frac{\partial L}{\partial r} = \left(\frac{\partial \mathbf{S}}{\partial r}\right)^{T} \mathbf{S} = \left(-\mathbf{B}\bar{\mathbf{f}}_{TS}\right)^{T} \left((\omega \mathbf{D} + \mathbf{A})\mathbf{y}_{TS} - r\mathbf{B}\bar{\mathbf{f}}_{TS}\right) = 0$$
(14b)

where $\bar{f}_{TS} = \frac{\partial f_{TS}}{\partial r} = \frac{f_{TS}}{r}$.

$$\begin{bmatrix} (\boldsymbol{D}\boldsymbol{y_{TS}})^{T}(\boldsymbol{D}\boldsymbol{y_{TS}}) & -(\boldsymbol{D}\boldsymbol{y_{TS}})^{T}(\boldsymbol{B}\bar{\boldsymbol{f}_{TS}}) \\ -(\boldsymbol{B}\bar{\boldsymbol{f}_{TS}})^{T}(\boldsymbol{D}\boldsymbol{y_{TS}}) & (\boldsymbol{B}\bar{\boldsymbol{f}_{TS}})^{T}(\boldsymbol{B}\bar{\boldsymbol{f}_{TS}}) \end{bmatrix} \begin{Bmatrix} \omega \\ r \end{Bmatrix} = \begin{Bmatrix} -(\boldsymbol{D}\boldsymbol{y_{TS}})^{T}(\boldsymbol{A}\boldsymbol{y_{TS}}) \\ (\boldsymbol{B}\bar{\boldsymbol{f}_{TS}})^{T}(\boldsymbol{A}\boldsymbol{y_{TS}}) \end{Bmatrix}$$
(15)

${\it 3.3. Fluid structure\ interaction\ and\ implementation}$

The fluid and structural domains are coupled by transferring the aerodynamic loads from the CFD solver to the structural solver and transferring the structural displacement and velocity from the structural solver to CFD solver using a staggered approach. The structural displacement and velocity are transferred to the fluid domain by deforming the CFD mesh as a rigid body, i.e., the translational and rotational displacement arising from the structural states are appropriately transferred to each CFD mesh point. Also, due to aerodynamics being more complex, multiple iteration of the CFD solver are carried out for each structural iteration. In summary, the solution procedure to predict the flutter boundary is given by the following steps, the schematic of which is shown in Fig. 1.

1) Initialize $[w_0, y_0, \omega_0, r_0], k \leftarrow 0, l \leftarrow 0.$

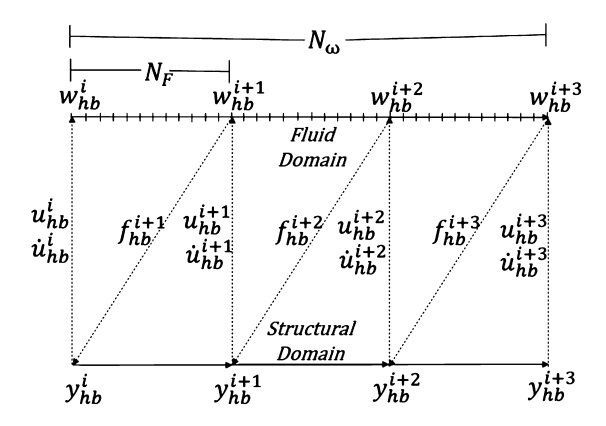


Fig. 1. Coupling of the fluid and structural domain.

2) Update w_{TS} from the aerodynamic analysis,

$$\frac{\Delta w_{TS}}{\Delta \tau} + \omega D w_{TS}^k V_{TS} + R_{TS} (w_{TS}^k) = 0$$

$$w_{TS}^{k+1} = w_{TS}^k + \Delta w_{TS}$$

- 3) Transfer aerodynamic force, f_{TS}^{k+1} , to the structural system after N_F aerodynamics solution iterations.
- 4) Update y_{TS} from the structural analysis,

$$\frac{\Delta y_{TS}}{\Delta \tau} + (\omega D + A) y_{TS}^{k+1} - B f_{TS}^{k} = 0$$
$$y_{TS}^{k+1} = y_{TS}^{k} + \Delta y_{TS}$$

5) Scale y_{TS} to satisfy the energy constraint.

$$y_{TS}^{k+1} = \frac{y_{TS}^{k+1}}{\sqrt{\frac{E_{avg}}{E_0}}}$$

- 6) Set $y_i = 0$, where i is any single index in $\{1, 2, ..., N_s\}$ and N_s is the total number of degrees of freedom.
- 7) Transfer structural deformation and velocity to the CFD domain.
- 8) Update ω and r by solving Eq. (15), after N_{ω} aero iterations.
- 9) Keep repeating steps 2)-7), until fluid and structural residuals converge.

It should be noted that, by constraining the structural energy to be low enough, a periodic solution at the flutter boundary can be obtained. Different LCO velocities can be obtained at other higher energy levels. The proposed method works to obtain unique solutions at different energy levels.

4. Time-spectral adjoint formulation for flutter and LCO problems

4.1. Derivation of the adjoint equations for sensitivity analysis

The flutter and the LCO solutions are not only governed by the coupled aero-structural equations, but also requires additional equations to determine ω and r respectively. These additional equations are the two constraint equations mentioned in the previous section: $Y(y) = y_i = 0$ and $E(y) = E_{avg}(y) - E_0 = 0$, respectively. A set of equations needed to solve the flutter and the LCO problems are denoted by R, S, Y and E, which are for aerodynamics, structures, a fixed structural state, and the total energy, respectively. The derivation of the adjoint equations should include the four coupled governing equations.

Considering that the cost function is defined by

$$I = I(\boldsymbol{w}, \boldsymbol{y}, \omega, r, \boldsymbol{b}), \tag{16}$$

where \boldsymbol{w} is the flow state, \boldsymbol{y} is the structural state, ω is the frequency of the periodic solution, r is the freestream parameter and \boldsymbol{b} are the design variables. Thus the total gradient of the cost function with respect to the design variables is given as,

$$\frac{dI}{d\mathbf{b}} = \frac{\partial I}{\partial \mathbf{b}} + \frac{\partial I}{\partial \mathbf{w}} \frac{d\mathbf{w}}{d\mathbf{b}} + \frac{\partial I}{\partial \mathbf{v}} \frac{d\mathbf{y}}{d\mathbf{b}} + \frac{\partial I}{\partial \omega} \frac{d\omega}{d\mathbf{b}} + \frac{\partial I}{\partial r} \frac{dr}{d\mathbf{b}}.$$
(17)

Similarly, the aerodynamics, structures and the constraint equations are function of the same state and design variables which are coupled in a nonlinear way. The total derivative of the equations with respect to the design variables are given by eqs. (18), (19), (20) and (21) respectively. These derivatives should always be zero irrespective of any changes in the design variables, as the residuals of the equations are zero upon convergence.

$$\frac{d\mathbf{R}}{d\mathbf{b}} = \frac{\partial \mathbf{R}}{\partial \mathbf{b}} + \frac{\partial \mathbf{R}}{\partial \mathbf{w}} \frac{d\mathbf{w}}{d\mathbf{b}} + \frac{\partial \mathbf{R}}{\partial \mathbf{y}} \frac{d\mathbf{y}}{d\mathbf{b}} + \frac{\partial \mathbf{R}}{\partial \omega} \frac{d\omega}{\partial \mathbf{b}} + \frac{\partial \mathbf{R}}{\partial r} \frac{dr}{d\mathbf{b}} = 0$$
(18)

$$\frac{d\mathbf{S}}{d\mathbf{b}} = \frac{\partial \mathbf{S}}{\partial \mathbf{b}} + \frac{\partial \mathbf{S}}{\partial \mathbf{w}} \frac{d\mathbf{w}}{d\mathbf{b}} + \frac{\partial \mathbf{S}}{\partial \mathbf{v}} \frac{d\mathbf{y}}{d\mathbf{b}} + \frac{\partial \mathbf{S}}{\partial \omega} \frac{d\omega}{\partial \mathbf{b}} + \frac{\partial \mathbf{S}}{\partial r} \frac{dr}{d\mathbf{b}} = 0$$
(19)

$$\frac{dY}{d\mathbf{b}} = \frac{\partial Y}{\partial \mathbf{b}} + \frac{\partial Y}{\partial \mathbf{w}} \frac{d\mathbf{w}}{d\mathbf{b}} + \frac{\partial Y}{\partial \mathbf{v}} \frac{d\mathbf{y}}{d\mathbf{b}} + \frac{\partial Y}{\partial \mathbf{w}} \frac{d\omega}{\partial \mathbf{b}} + \frac{\partial Y}{\partial r} \frac{dr}{d\mathbf{b}} = 0$$
(20)

$$\frac{dE}{d\mathbf{b}} = \frac{\partial E}{\partial \mathbf{b}} + \frac{\partial E}{\partial \mathbf{w}} \frac{d\mathbf{w}}{d\mathbf{b}} + \frac{\partial E}{\partial \mathbf{v}} \frac{d\mathbf{y}}{d\mathbf{b}} + \frac{\partial E}{\partial \omega} \frac{d\omega}{\partial \mathbf{b}} + \frac{\partial E}{\partial r} \frac{dr}{d\mathbf{b}} = 0$$
(21)

Since the total derivatives of the governing equations are zero, an individual equation can be multiplied by a Lagrangian multiplier and freely added to the cost function derivative. Introducing the Lagrange multipliers of ψ , ϕ , θ and η for aerodynamics, structures, a phase constraint, and the energy constraint, respectively, the derivative of the cost function is re-written as

$$\frac{dI}{d\mathbf{b}} = \frac{\partial I}{\partial \mathbf{b}} + \frac{\partial I}{\partial \mathbf{w}} \frac{d\mathbf{w}}{d\mathbf{b}} + \frac{\partial I}{\partial \mathbf{y}} \frac{d\mathbf{y}}{d\mathbf{b}} + \frac{\partial I}{\partial \omega} \frac{d\omega}{d\mathbf{b}} + \frac{\partial I}{\partial r} \frac{dr}{d\mathbf{b}} + \boldsymbol{\psi}^{T} \left(\frac{\partial \mathbf{R}}{\partial \mathbf{b}} + \frac{\partial \mathbf{R}}{\partial \mathbf{w}} \frac{d\mathbf{w}}{d\mathbf{b}} + \frac{\partial \mathbf{R}}{\partial \mathbf{y}} \frac{d\mathbf{y}}{d\mathbf{b}} + \frac{\partial \mathbf{R}}{\partial \mathbf{w}} \frac{d\mathbf{y}}{d\mathbf{b}} + \frac{\partial \mathbf{S}}{\partial \mathbf{w}} \frac{d\mathbf{w}}{d\mathbf{b}} + \frac{\partial \mathbf{S}}{\partial \omega} \frac{d\omega}{\partial \mathbf{b}} + \frac{\partial \mathbf{S}}{\partial r} \frac{dr}{d\mathbf{b}} \right) + \boldsymbol{\theta}^{T} \left(\frac{\partial Y}{\partial \mathbf{b}} + \frac{\partial Y}{\partial \mathbf{w}} \frac{d\mathbf{w}}{d\mathbf{b}} + \frac{\partial Y}{\partial \mathbf{w}} \frac{d\mathbf{w}}{d\mathbf{b}} + \frac{\partial Y}{\partial \omega} \frac{d\omega}{\partial \mathbf{b}} + \frac{\partial Y}{\partial r} \frac{dr}{d\mathbf{b}} \right) + \boldsymbol{\eta}^{T} \left(\frac{\partial E}{\partial \mathbf{b}} + \frac{\partial E}{\partial \mathbf{w}} \frac{d\mathbf{w}}{d\mathbf{b}} + \frac{\partial E}{\partial \mathbf{w}} \frac{d\omega}{d\mathbf{b}} + \frac{\partial E}{\partial \omega} \frac{d\omega}{d\mathbf{b}} + \frac{\partial E}{\partial r} \frac{dr}{d\mathbf{b}} \right) \tag{22}$$

The expression can be re-arranged in Eq. (23) such that the terms of the residual variation with respect to the design variables are factored together into a single bracket. By setting the terms within the brackets to zero, the total derivative of the cost function becomes independent of the variation of the state residual with respect to the state variables. This is because the variation of the residuals is affected by the changes in state variables as well as those in the design variables, and requires the solution of the entire governing equations for each design variable, which makes the sensitivity analysis computationally expensive. Thus, the equations of the discrete adjoint variables are obtained in Eq. (24) after the terms within the brackets in Eq. (23) are set to zero.

$$\frac{dI}{d\mathbf{b}} = \frac{\partial I}{\partial \mathbf{b}} + \boldsymbol{\psi}^{T} \frac{\partial \mathbf{R}}{\partial \mathbf{b}} + \boldsymbol{\phi}^{T} \frac{\partial \mathbf{S}}{\partial \mathbf{b}} + \boldsymbol{\theta}^{T} \frac{\partial \mathbf{Y}}{\partial \mathbf{b}} + \boldsymbol{\eta}^{T} \frac{\partial E}{\partial \mathbf{b}} + \left(\frac{\partial I}{\partial \mathbf{w}} + \boldsymbol{\psi}^{T} \frac{\partial \mathbf{R}}{\partial \mathbf{w}} + \boldsymbol{\phi}^{T} \frac{\partial \mathbf{S}}{\partial \mathbf{w}} + \boldsymbol{\theta}^{T} \frac{\partial Y}{\partial \mathbf{w}} + \boldsymbol{\eta}^{T} \frac{\partial E}{\partial \mathbf{w}}\right) \frac{d\mathbf{w}}{d\mathbf{b}} + \left(\frac{\partial I}{\partial \mathbf{y}} + \boldsymbol{\psi}^{T} \frac{\partial \mathbf{R}}{\partial \mathbf{y}} + \boldsymbol{\phi}^{T} \frac{\partial \mathbf{S}}{\partial \mathbf{y}} + \boldsymbol{\theta}^{T} \frac{\partial Y}{\partial \mathbf{y}} + \boldsymbol{\eta}^{T} \frac{\partial E}{\partial \mathbf{y}}\right) \frac{d\mathbf{y}}{d\mathbf{b}} + \left(\frac{\partial I}{\partial \omega} + \boldsymbol{\psi}^{T} \frac{\partial \mathbf{R}}{\partial \omega} + \boldsymbol{\phi}^{T} \frac{\partial \mathbf{S}}{\partial \omega} + \boldsymbol{\theta}^{T} \frac{\partial Y}{\partial \omega} + \boldsymbol{\eta}^{T} \frac{\partial E}{\partial \omega}\right) \frac{d\omega}{d\mathbf{b}} + \left(\frac{\partial I}{\partial r} + \boldsymbol{\psi}^{T} \frac{\partial \mathbf{R}}{\partial r} + \boldsymbol{\phi}^{T} \frac{\partial \mathbf{S}}{\partial r} + \boldsymbol{\theta}^{T} \frac{\partial Y}{\partial r} + \boldsymbol{\eta}^{T} \frac{\partial E}{\partial r}\right) \frac{dr}{d\mathbf{b}}$$

$$(23)$$

$$\begin{bmatrix} \frac{\partial \mathbf{R}}{\partial \mathbf{w}} & \frac{\partial \mathbf{R}}{\partial \mathbf{y}} & \frac{\partial \mathbf{R}}{\partial \omega} & \frac{\partial \mathbf{R}}{\partial r} \\ \frac{\partial \mathbf{S}}{\partial \mathbf{w}} & \frac{\partial \mathbf{S}}{\partial \mathbf{y}} & \frac{\partial \mathbf{S}}{\partial \omega} & \frac{\partial \mathbf{S}}{\partial r} \\ \frac{\partial \mathbf{Y}}{\partial \mathbf{w}} & \frac{\partial \mathbf{Y}}{\partial \mathbf{y}} & \frac{\partial \mathbf{Y}}{\partial \omega} & \frac{\partial \mathbf{Y}}{\partial r} \\ \frac{\partial \mathbf{E}}{\partial \mathbf{w}} & \frac{\partial \mathbf{E}}{\partial \mathbf{y}} & \frac{\partial \mathbf{E}}{\partial \omega} & \frac{\partial \mathbf{E}}{\partial r} \end{bmatrix}^{T} \begin{bmatrix} \boldsymbol{\psi} \\ \boldsymbol{\phi} \\ \boldsymbol{\theta} \\ \boldsymbol{\eta} \end{bmatrix} = - \begin{bmatrix} \frac{\partial I}{\partial \mathbf{w}} \\ \frac{\partial I}{\partial \mathbf{y}} \\ \frac{\partial I}{\partial \omega} \\ \frac{\partial I}{\partial r} \end{bmatrix}$$

$$(24)$$

Then, the final form of the variation of the cost function can be written as follows in Eq. (25). Increase in the size of the vector of the design variables affects only the residuals, not the state variables, which is the major advantage of the discrete adjoint solution method.

$$\frac{dI}{d\mathbf{b}} = \frac{\partial I}{\partial \mathbf{b}} + \boldsymbol{\psi}^{T} \frac{\partial \mathbf{R}}{\partial \mathbf{b}} + \boldsymbol{\phi}^{T} \frac{\partial \mathbf{S}}{\partial \mathbf{b}} + \boldsymbol{\theta}^{T} \frac{\partial Y}{\partial \mathbf{b}} + \boldsymbol{\eta}^{T} \frac{\partial E}{\partial \mathbf{b}}$$
(25)

4.2. Jacobian sub-matrices of the adjoint equations

$$\frac{\partial \mathbf{R}}{\partial \mathbf{v}} = \frac{\partial \mathbf{R}}{\partial \mathbf{s}} \frac{\partial \mathbf{s}}{\partial \mathbf{x}_{\mathbf{v}}} \frac{\partial \mathbf{x}_{\mathbf{v}}}{\partial \mathbf{x}_{\mathbf{s}}} \frac{\partial \mathbf{x}_{\mathbf{s}}}{\partial \mathbf{v}} \tag{26}$$

The Jacobian $\frac{\partial \mathbf{R}}{\partial r}$ can be computed in a similar fashion. While the convective flux doesn't depend on the freestream parameter inside the domain, the flux for the cells at farfield boundary would depend on the freestream parameter due to the farfield boundary condition (which has been defined as characteristic boundary condition, additional details for it can be found here [36]). Change in the farfield parameter would result in change in the flow variables of the ghost cells, which would then translate to change in the flux of the cells along the farfield boundary. Therefore, the vector $\frac{\partial \mathbf{R}}{\partial r}$ would be non-zero only at the cells along the farfield boundary and can be calculated using the chain rule expression given by Eq. (27).

$$\frac{\partial R}{\partial r} = \begin{cases} \frac{\partial R_i}{\partial r} = \frac{\partial R_i}{\partial \mathbf{w_G}} \frac{\partial \mathbf{w_G}}{\partial r} & \text{if } i \in \text{Farfield} \\ \frac{\partial R_i}{\partial r} = 0 & \text{if } i \in \text{elsewhere} \end{cases}$$
 (27)

The structural residual also isn't explicitly a function of the fluid state, but a function through the boundary condition. Changes in the fluid state would lead to change in the pressure distribution on the wing, which in turn would lead to changes aerodynamic force vector acting on the structure. Hence, the Jacobian, $\frac{\partial S}{\partial w}$, is also computed by chain rule based differentiation and is given by (28). The partial derivatives required in the Eqs. (26), (27) and (28) have been computed using algorithmic differentiation. While simpler subroutines have been differentiated manually and Tapenade [38] has been used to differentiate long and complex subroutines.

$$\frac{\partial \mathbf{S}}{\partial \mathbf{w}} = \frac{\partial \mathbf{S}}{\partial \mathbf{f}} \frac{\partial \mathbf{f}}{\partial \mathbf{p}} \frac{\partial \mathbf{p}}{\partial \mathbf{w}} \tag{28}$$

Most of the remaining Jacobian matrices can also be computed due their explicit dependence on the state variables. They are given by Eq. (29).

$$\frac{\partial \mathbf{R}}{\partial \omega} = \mathbf{D}\mathbf{w} \tag{29a}$$

$$\frac{\partial \mathbf{S}}{\partial \omega} = \mathbf{D} \mathbf{y} \tag{29b}$$

$$\frac{\partial \mathbf{S}}{\partial r} = -\mathbf{B}\bar{\mathbf{f}} \tag{29c}$$

$$\frac{\partial Y}{\partial \mathbf{w}} = 0 \tag{29d}$$

$$\frac{\partial \mathbf{Y}}{\partial \mathbf{v}} = [0 \quad 0 \quad \dots \quad 1 \quad \dots \quad 0] \tag{29e}$$

$$\frac{\partial Y}{\partial \omega} = 0 \tag{29f}$$

$$\frac{\partial Y}{\partial r} = 0 \tag{29g}$$

$$\frac{\partial E}{\partial \mathbf{w}} = 0 \tag{29h}$$

$$\frac{\partial E}{\partial \mathbf{y}} = \mathbf{G}\mathbf{y} \tag{29i}$$

$$\frac{\partial E}{\partial \omega} = 0 \tag{29j}$$

$$\frac{\partial E}{\partial r} = 0 \tag{29k}$$

5. Results

5.1. Implementation and validation

The three-dimensional, compressible Navier-Stokes flow solver Stanford University multi-block (SUmb) was used for the aerodynamic analysis in this study. SUmb is a multi-block, structured grid flow solver that was developed at Stanford University under the sponsorship of the Department of Energy Advanced Strategic Computing program. It is a massively parallel code (in both CPU and memory) that uses a METIS based mesh partitioning, load balancing, and Message Passing Interface for parallelization. For steady/time-spectral calculations, the multistep Runge-Kutta time stepping is used to march to the steady/periodic steady state in pseudo time. For time-accurate calculations, dual time stepping with 2nd and 3rd order backward difference formula can be used. Spatial discretization can be carried out by using a central difference scheme (second-order in space) with several artificial dissipation options (scalar, matrix or Convective Upwind Split Pressure) or upwind schemes such as Roe's Flux Difference Splitting or Van Leer's Flux Vector Splitting schemes. Additional details regarding the solver can be found here [39]. In this study, a second-order Backward Differentiation Formula scheme was used for the time-accurate computation, and central difference scheme with scalar artificial dissipation was used for the convective fluxes.

For the adjoint based sensitivity analysis, due to the sparsity of the adjoint matrix, the PetSc toolkit is utilized to efficiently store the non-zero entries of the matrix as well as use its advanced linear algebra capabilities to solve the system. For this study, the adjoint matrix has a size of \sim 57,600. Restarted GMRES [40] was used to solve the adjoint equations along with incomplete LU decomposition being used as the preconditioner and the method being restarted every 300 iterations. Overall, it took \sim 1,000 iterations to converge.

The developed flutter prediction scheme was first validated for the AGARD test case, where the flutter onset conditions were computed for the AGARD 445.6 wing at different Mach numbers and computed with the experimental results. The details of the validation study haven't been presented here and interested readers can check here [41].

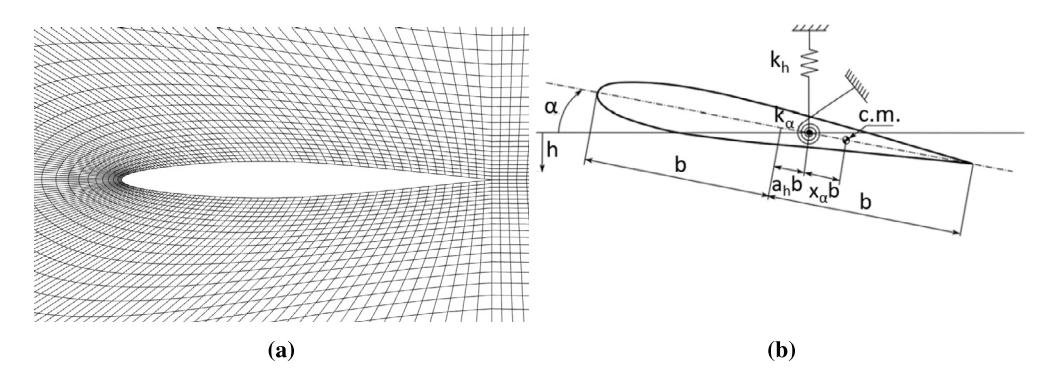


Fig. 2. (a) CFD mesh used in the study. (b) Structural schematic of the pitch/plunge airfoil used.

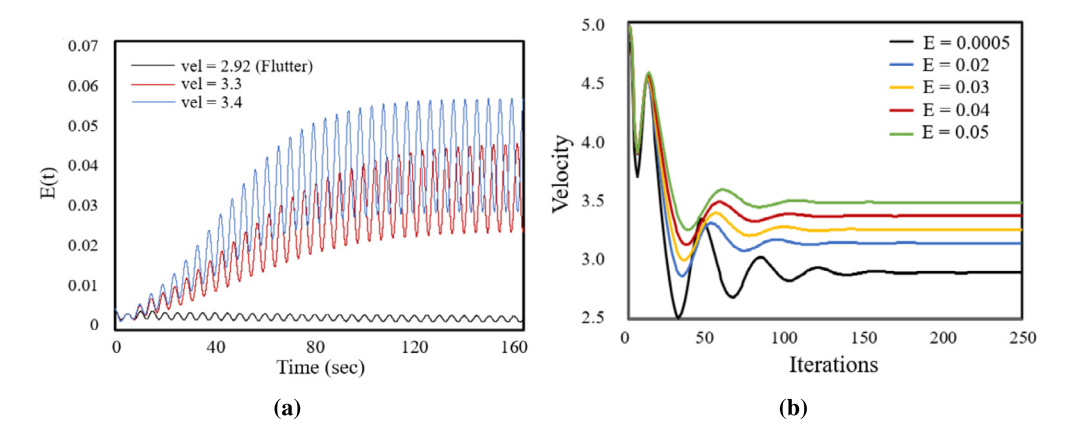


Fig. 3. (a) Time accurate response of energy for different freestream velocity (b) Convergence history for different energy constraint levels using the time-spectral approach with one harmonic. (For interpretation of the colors in the figure(s), the reader is referred to the web version of this article.)

5.2. Prediction of flutter and LCO conditions

The proposed flutter and LCO prediction was applied to the pitch-plunge airfoil section. The CFD mesh used in this case (251×51 grid points) is shown in Fig. 2a. The corresponding structural schematic is shown in Fig. 2b. The airfoil has the NACA 64A010 cross section. The Mach number of the flow was 0.8 and the airfoil section was placed at a zero angle of attack.

The flutter and LCO solutions were first analyzed using the time accurate approach, where the unsteady governing equations were solved for different freestream velocities. The energy response of $E(t) = \frac{1}{2}(\boldsymbol{u}(t)^T \boldsymbol{K} \boldsymbol{u}(t) + \dot{\boldsymbol{u}}(t)^T \boldsymbol{M} \dot{\boldsymbol{u}}(t))$ for different velocities can be seen in Fig. 3a with respect to different flutter velocity. With the time accurate approach, the flutter boundary was observed at $V_F = 2.92$. Similarly, flutter and LCO solutions were obtained by constraining the average energy levels to different values. The convergence history of the freestream velocity with a single harmonic is shown in Fig. 3b. It can be seen that as the energy constraint is set to different levels, the velocity converges to different values.

The average energy for both, the time-accurate and the time-spectral methods, is shown in Fig. 4a and 4b for different LCO velocity and frequency, respectively. The number of harmonics for the time-spectral method was varied from one to six. For the time-spectral method with one and two harmonics, the solution does not match well with the solution from the time-accurate method, especially at higher energy levels. For the single harmonic time-spectral case, the velocity and frequency are under-predicted, whereas for two harmonics, they are over-predicted. Overall, as the number of harmonics were increased for the time-spectral solution, the velocity and frequency predictions were more accurate and matched better with the time-accurate results. For example, the time-spectral solution obtained using three harmonics shows higher accuracy than the solution obtained using two harmonics, but is less accurate than the solution obtained using four or higher harmonics. This indicates that the LCOs with greater displacement amplitudes require more time instances to accurately capture the non-linear physics, while the flutter boundary can be computed for sufficient accuracy with just a single harmonic. Also, both Fig. 4a and 4b are linear at small energy levels. However, as the energy level is increased and LCOs at higher energy levels are considered, the non-linear shock motion becomes stronger and that is reflected in the two plots.

Fig. 5a plots the plunge displacement versus the plunge velocity, while Fig. 5b plots the pitch angle versus the pitching rate, for both time accurate and time-spectral cases. The average structural energy in these plots is $E_{avg}=0.05$. These plots reflect the same observations that were made in Fig. 4. The time-spectral results obtained using one and two harmonics do not match the time accurate results as accurately as results obtained using higher harmonics. While the results from the time accurate and time-spectral methods show good agreements in Fig. 5a, the same is not true in Fig. 5b. For Fig. 5b, the time-spectral results with one harmonic under-predict the pitch angle and rate, while the time-spectral results with two harmonics over-predict them, when compared to time accurate results. However, time-spectral results with higher harmonics match the time accurate results with greater accuracy.

Fig. 6 compares the airfoil pressure distribution, obtained using the time-spectral and time-accurate methods, at different phase angles over the period of the periodic cycle. The time-spectral solution used in this figure was obtained using five harmonics. It can be seen that the time-spectral and time accurate solution match considerably well with each other except at $\phi = \frac{2\pi}{11}1$ and $\frac{2\pi}{11}7$ rads in Figs. 6a and 6d.

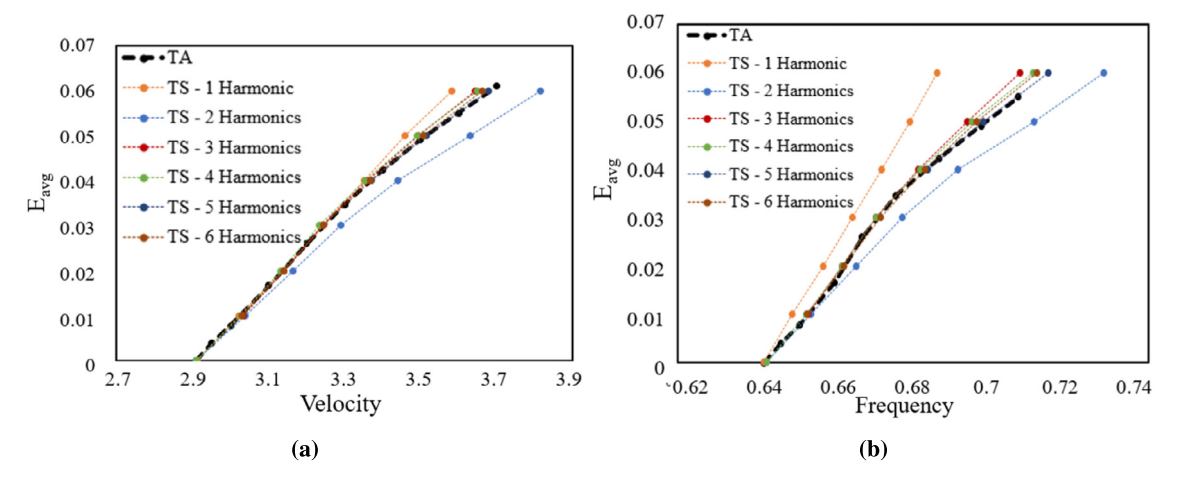


Fig. 4. (a) Average energy versus freestream velocity (b) Average energy vs LCO frequency.

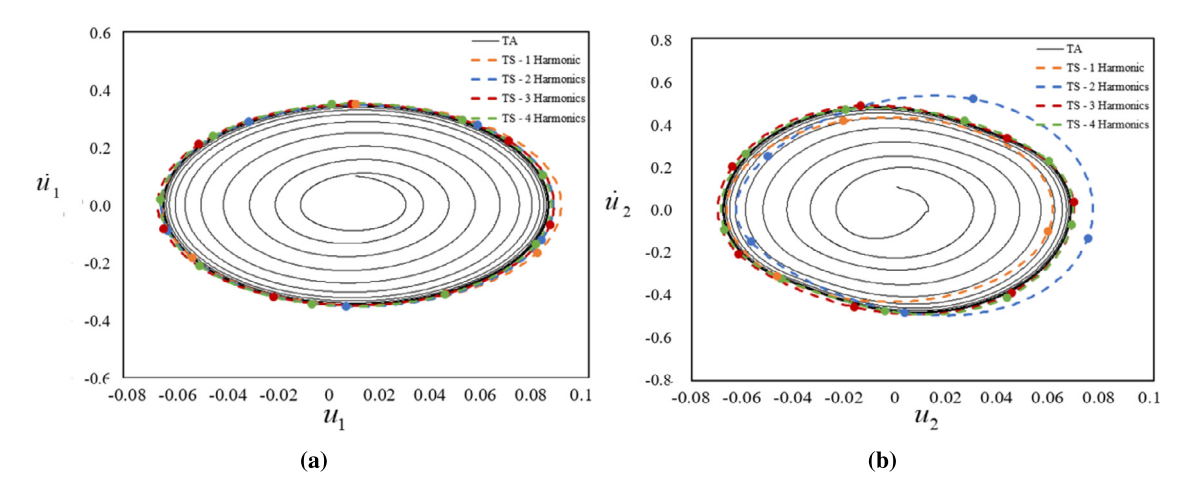


Fig. 5. (a) u_1 versus \dot{u}_1 (b) u_2 versus \dot{u}_2 for $E_{avg} = 0.05$.

The corresponding pressure coefficient contour plots from the time-spectral results are shown in Fig. 7. From these corresponding plots, it can be seen that the discrepancy between the time-spectral and time-accurate solutions arises when weak shock exists on both, the upper and the lower surfaces, or the shock is transitioning from one surface to another. The physics in this case is too complex for the time-spectral method with smaller number of harmonics to capture accurately. Hence, additional collocation points are required in the time-spectral solution to accurately capture the flow solution. The minor discrepancies observed in Fig. 4 can be attributed to this.

5.3. Adjoint sensitivity analysis

The Hicks Henne [37] bump functions were used to parameterize the airfoil shape, with the amplitudes of the bumps being the design variables. Instead of having two separate set of bump functions for the upper and lower surface, a single set of twenty four bump functions were evenly distributed along the airfoil, starting from the lower trailing edge, encircling the airfoil in an anti-clockwise fashion, and ending at the upper trailing edge. This approach enables better exploration of the airfoil shape, especially near the leading edge as more bump functions can be placed in that region. However, the downside of this approach is that the bump functions modify the airfoil shape in a slightly asymmetric fashion. A sample bump function acting on the airfoil surface is shown in Fig. 8a and the amplitude was exaggerated for visualization purpose. The sensitivity of LCO velocity at E_{avg} of 0.02, with respect to the coefficients of twenty four bump functions, was computed using both the finite difference and the coupled adjoint solution approach, and the results are shown in Fig. 8b. For the finite difference study, a step size study was carried out and for comparison, a step size of 0.01% of the chord length was considered. Good agreements are observed in the gradient values calculated by the two approaches with the maximum error being less than 2%. In Fig. 8b, the LCO velocity is found to be sensitive to the airfoil shape change near the mid-chord and leading edge areas. This is due to the airfoil shape modifying the shock strength and location. The same has been reflected in the design results and is discussed in detail in the next section. As the flow is symmetric, the flutter/LCO velocity sensitivity should also be symmetric as well. However, that is not the case as seen in Fig. 8b and this can be attributed to the Hicks-Henne bump function parameterization that modifies the airfoil shape in an asymmetric manner. This asymmetry translates into a slight asymmetry in the sensitivity which in turn translates into asymmetry in the optimized airfoils presented in the study. The reader can overcome this by having a shape parameterization approach that allows for symmetric changes to the airfoil shape.

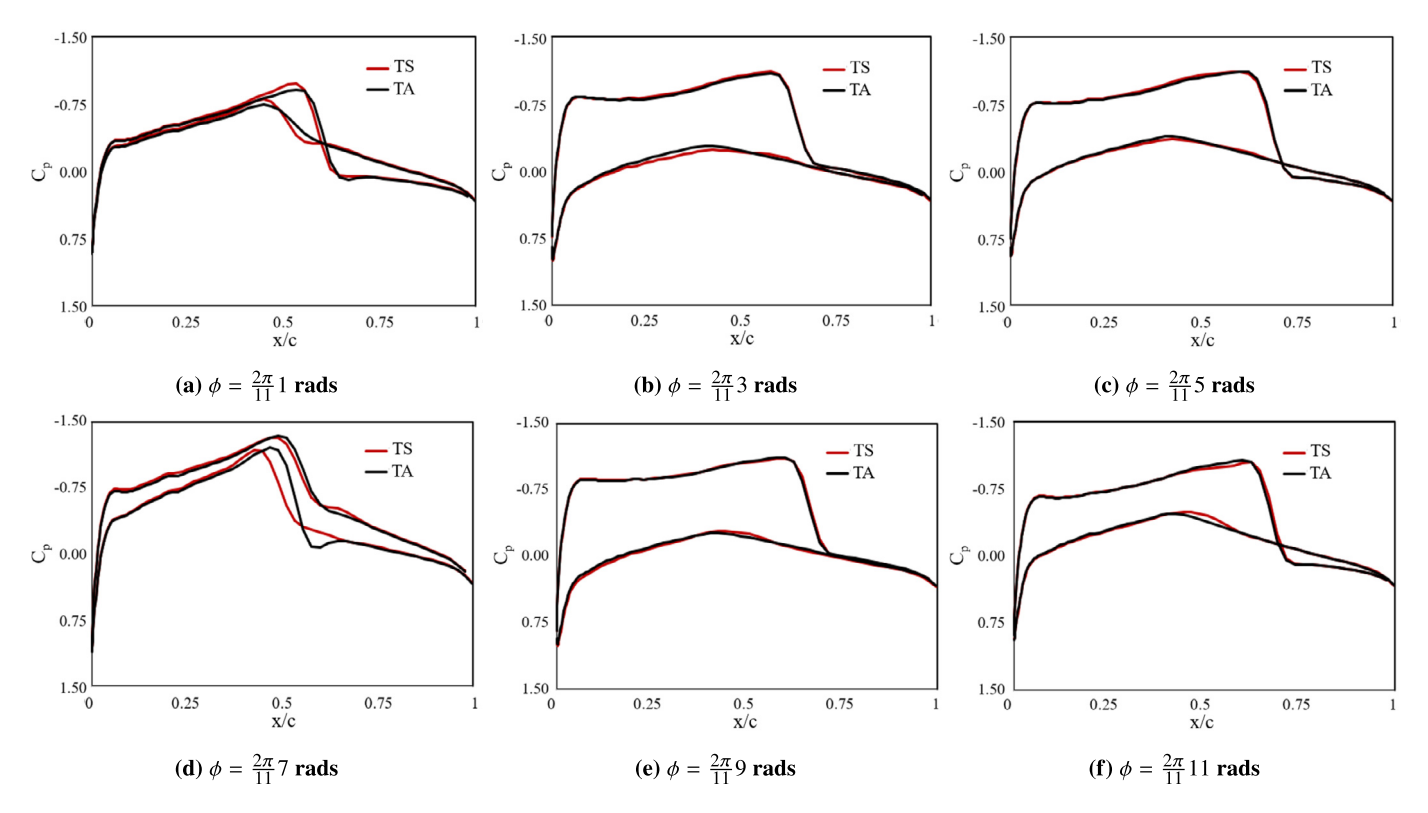


Fig. 6. Pressure coefficient distribution on the airfoil surface at different phases over a period, calculated by time-accurate method (in red) and time-spectral method (in black) with five harmonics.

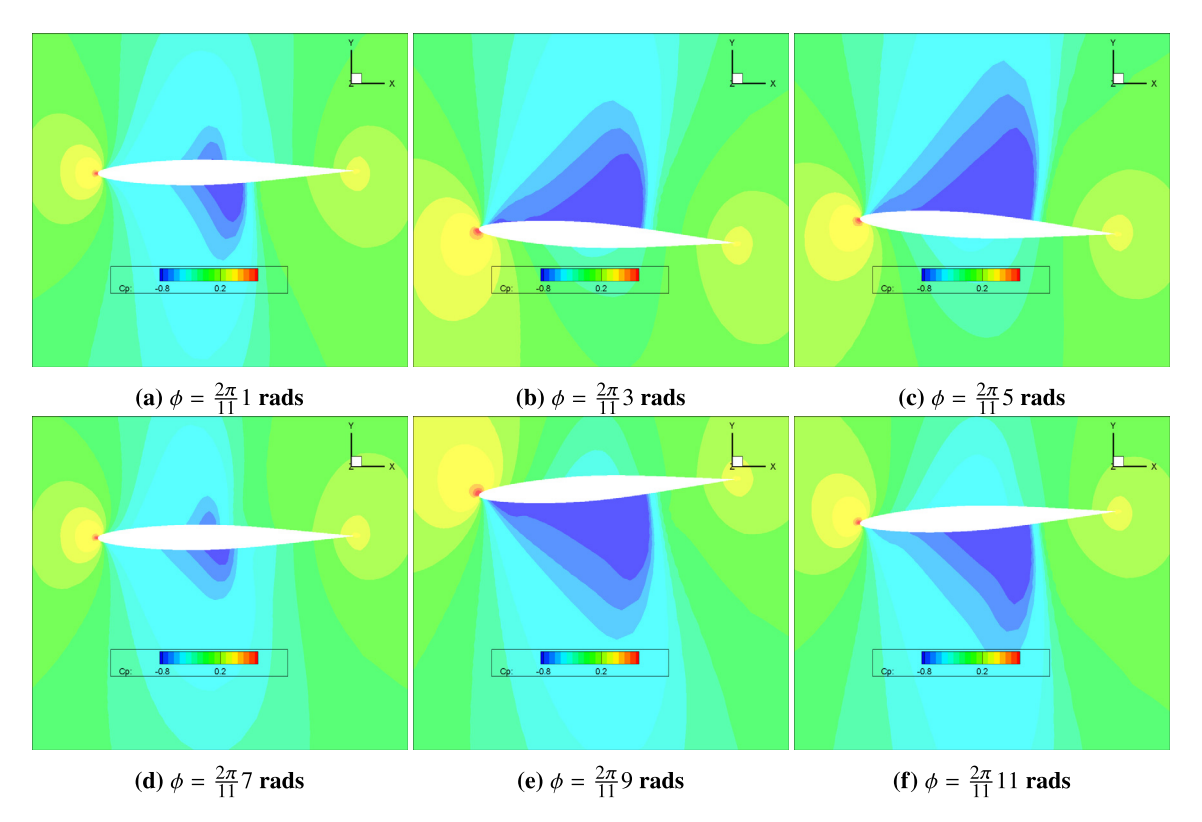


Fig. 7. Pressure coefficient contour at different phases over a period (TS method using five harmonics).

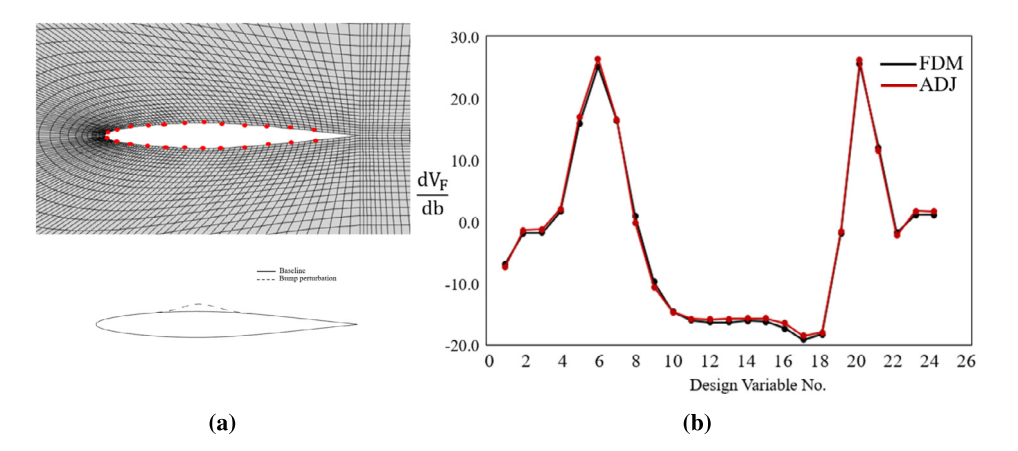


Fig. 8. (a) (Top) Location of amplitude for each Hicks Henne bump shown on the airfoil surface (Bottom) Perturbation in the airfoil shape shown due to a bump function. (b) Sensitivity of the LCO velocity w.r.t. the magnitude of the bump function ($E_{avg} = 0.02$).

5.4. Computational cost and numerical stability

Before presenting the optimization results, we briefly discuss the computational cost and numerical stability for the time-spectral approach. The time-spectral approach is generally found to be computationally more efficient than the time-accurate approach for periodic problems with known frequency. However, in our case, both the frequency and velocity were part of the solution scheme and the time-spectral method took more time than the time-accurate approach. For the airfoil problem discussed above, the time spectral approach took roughly 1.5-2 hours on a single CPU with a clock speed of 2.1 GHz, while the time accurate approach took 0.5 hours. But since the flow velocity is an input for the time-accurate approach and is not known apriori for the flutter prediction problem, it can take up to 2-3 runs to accurately pinpoint the flutter velocity. Hence, the time-spectral method for flutter prediction turns out to have approximately the same computational cost as the time-accurate method. However, predicting LCOs at a fixed velocity requires only one time-accurate approach and hence it is computationally more efficient than the time-spectral method. Moreover, the time-spectral approach can be numerically unstable at times, leading the solution to diverge. It thus requires numerical tuning at times, such as choosing appropriate numerical parameters such as initial conditions, pseudo-time step size, etc.

However, these shortcomings for an individual calculation are outweighed by the large time savings obtained during the optimization phase, by using the time spectral adjoint method for sensitivity analysis. It is significantly more efficient than finite difference based sensitivity analysis and requires much less memory than the time-accurate adjoint method.

5.5. Shape optimization results

Using the coupled adjoint based sensitivity analysis, the airfoil shape was optimized to delay the flutter onset conditions, by maximizing the flutter velocity. This was done with and without any constraint on the drag. First, the case without drag constraint was carried out. The optimization problem statement was as follows.

maximize
$$V_F$$

s.t $x_L < x_i < x_U, i = 1, 2, ..., N_X$

The bump function amplitude was bounded to 1.0% of the airfoil chord length. Low-storage BFGS [42], implemented in the NLOPT library [43], was used in this study. The optimize airfoil showed a 30% increase in flutter velocity. The final optimized airfoil is shown in Fig. 9a, along with the baseline airfoil. Compared to the baseline, the optimized airfoil is thicker near the mid section and becomes lean towards the front. This outcome is expected, based on the sensitivity plot shown in Fig. 8b, as the gradient of the flutter velocity is positive in the mid section and negative near the front. The corresponding LCO velocity profile is shown in Fig. 9b. A similar increase is observed throughout the entire velocity profile not just the flutter onset velocity. Fig. 10 compares the pressure coefficient distribution of the two airfoils, where the optimized airfoil has a stronger shock but is more aft compared to the baseline. This change in shock strength and location can be attributed to the decreased thickness near the leading edge and increased thickness in the mid section of the optimized airfoil. These changes in the airfoil surface lead to greater curvature. This in turn leads to greater expansion of the flow, a greater drop in the surface pressure and a stronger transonic shock. This effect is the opposite of the one seen in supercritical airfoils, which have a flat upper surface to reduce the shock strength. More on the effect of airfoil shape on transonic shocks can be found here [44]. However, the stronger shock of optimized airfoil increases its wave drag correspondingly, and it does not bear practical importance.

In order to further explore the cause of increase in the flutter onset velocity, both the baseline and optimized airfoils were analyzed using the p-k method. The aerodynamic derivatives matrix and the damping coefficient was computed at both, on and off the flutter velocity conditions. Fig. 11 shows the phase difference of the aerodynamic derivatives matrix coefficients at different reduced frequency, $k = \left(\frac{\omega b}{U}\right)$. From the figure, it can be seen that while the matrix coefficients involving the lift coefficient (Fig. 11a and Fig. 11b) are mildly affected by the change in shape, significant variation is observed for the matrix coefficients involving the moment coefficient (Fig. 11c and Fig. 11d). This can be attributed to the change in shock location, which in turn induces change in center of pressure, which in turn affects the moment coefficient.

The changes in the aerodynamic derivatives matrix are also reflected in the frequency and damping coefficient, as seen in Fig. 12, where they have been plotted as a function of the velocity. While the damping coefficient for both the airfoils is similar at lower reduced

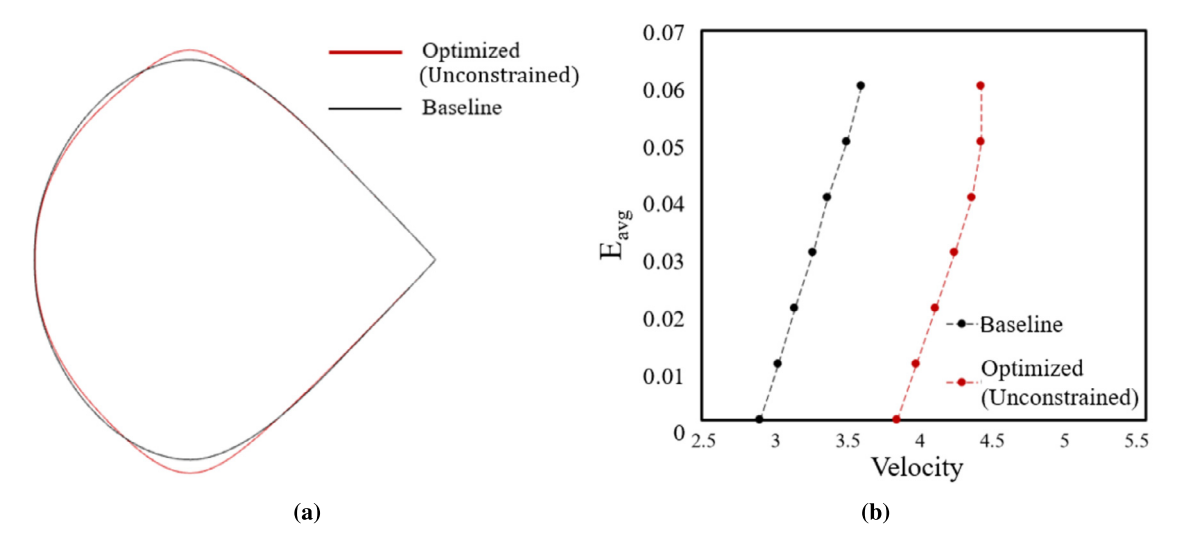


Fig. 9. (a) Comparison of baseline and optimized airfoil (b) Comparison of the LCO velocity profile for the baseline and optimized airfoil.

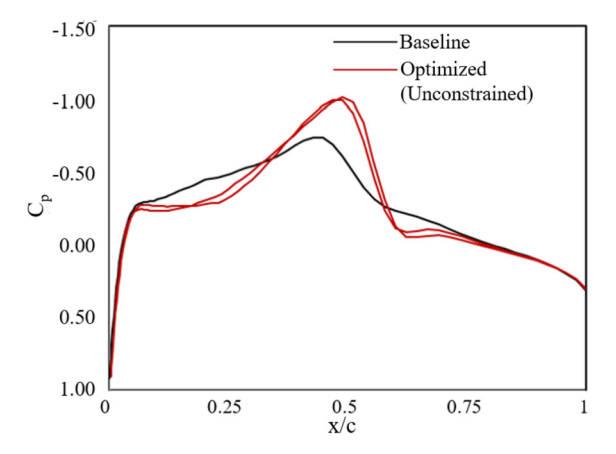


Fig. 10. Comparison of pressure coefficient distribution for the baseline and optimized airfoil.

frequencies, the rate of increase of the damping coefficient is slower for the optimized airfoil compared to the baseline airfoil. This leads to a higher flutter velocity for the optimized airfoil. Subsequently, the higher flutter onset velocity also leads to higher LCO velocities at different energy levels.

While the optimized airfoil had a substantially higher flutter velocity, it's drag coefficient was substantially higher than the baseline airfoil as well, increasing from 0.0055 to 0.0126. The increase in drag is not desirable and is due to the increase in the shock strength, which in turn is due to the increase in airfoil thickness. Since there was no constraint on the drag coefficient, the design optimization process resulted in an airfoil with much higher drag.

In order to avoid high drag, another design cycle was carried out with the drag coefficient being added as a weighted penalty term to the objective function. Correspondingly, the objective function was modified to $(-V_F/V_0) + \beta(C_D/C_{D0})$, where V_0 and C_{D0} are the flutter onset velocity and drag coefficient of the baseline airfoil. The weight coefficient, β , was set as 1.0, 1.1 and 1.2, to find different design candidates that had higher flutter velocity without exceeding the baseline drag. While the flutter velocity was determined by the time-spectral FSI approach discussed above, the drag coefficient was computed using the steady CFD solver, as we are primarily interested in having low drag during the regular operating conditions, not at the flutter or LCO conditions. The convergence history for $\beta = 1.1$ is shown in Fig. 13. As mentioned above, all the design candidates with drag greater than the baseline drag were ignored and only the feasible designs have been shown in the convergence history plot. From the figure, it can be seen that the last iteration shows the design candidate with the highest flutter velocity and has been considered as the optimal airfoil.

The optimized airfoil for the constrained optimization is shown in Fig. 14a, along with the baseline airfoil and the optimized airfoil from the unconstrained optimization. The optimized airfoil from the constrained optimization had a drag coefficient similar to the baseline airfoil of 0.0054. Compared to the unconstrained optimization case, the airfoil resulting from the constrained optimization has smaller thickness. Also, the position of the maximum thickness was more aft. Fig. 14b shows the corresponding LCO profile. Compared to the baseline, the optimized airfoil showed a 25% increase in flutter velocity and the corresponding LCO velocity profile. Fig. 15 compares the airfoil pressure coefficient distribution for the baseline, the constrained optimization airfoil and the unconstrained optimization airfoil. Since the constrained optimization airfoil is leaner than the unconstrained optimization airfoil, the former's shock strength is weaker compared to the latter. However, as its maximum thickness location is more aft compared to the baseline, so is the shock location. Hence, it can be concluded that compared to the unconstrained optimization case, the smaller thickness from the constrained optimization case lead to a lower drag, while the more aft location of the maximum thickness/shock lead to favorable flutter characteristics compared to the baseline airfoil.

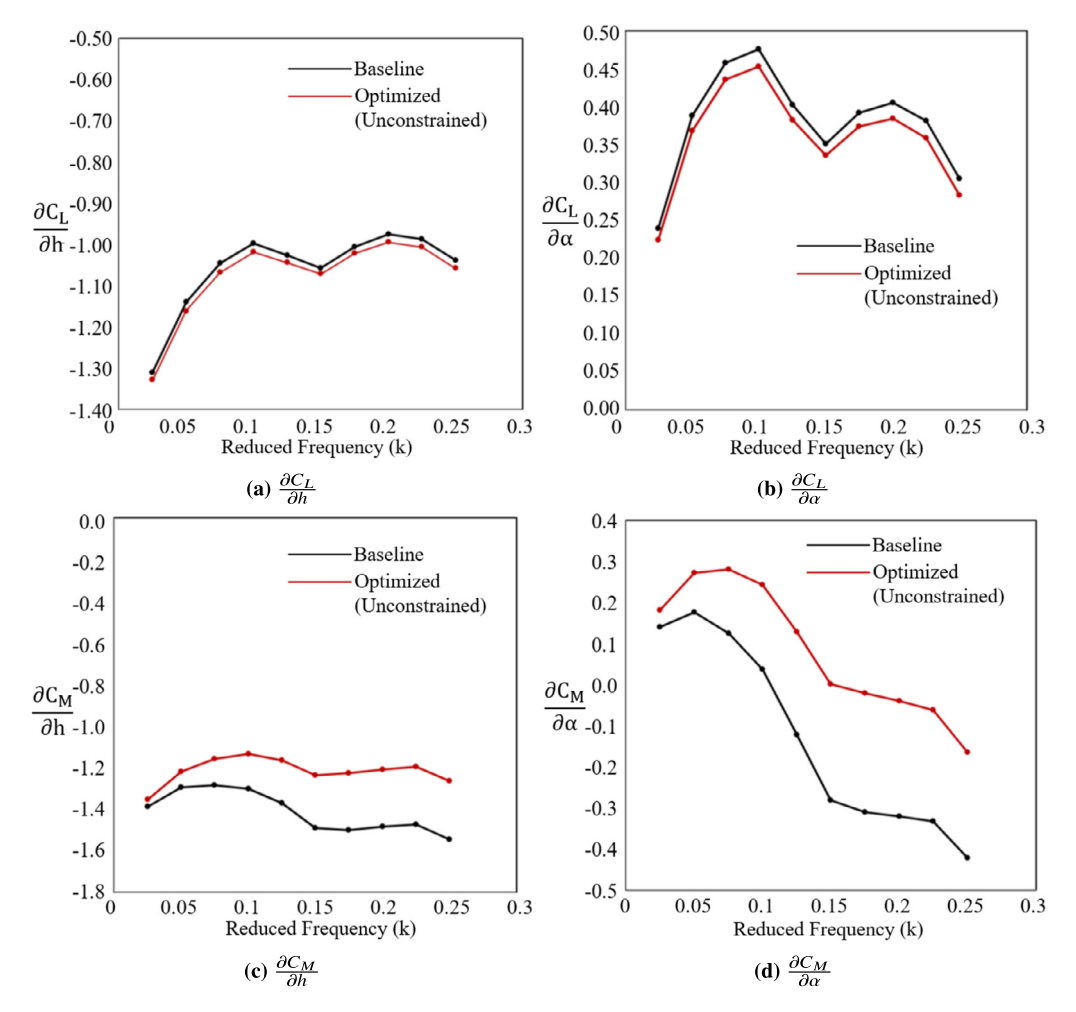


Fig. 11. Phase of aerodynamic derivates matrix coefficients at varying reduced frequency (k).

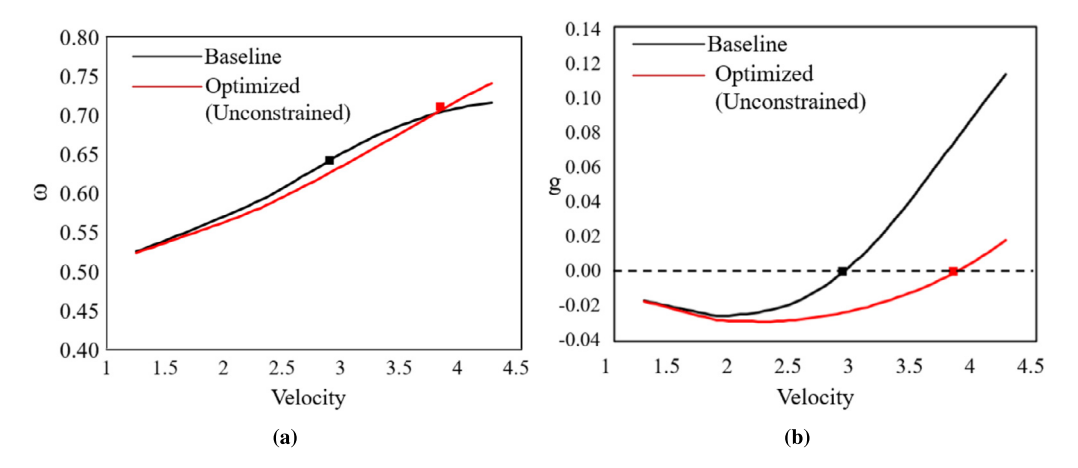


Fig. 12. Comparison of (a) frequency and (b) damping coefficient for the baseline and the optimized airfoil.

The p-k method was also applied to the airfoil obtained from the constrained optimization. The aerodynamic derivatives matrix coefficients for the optimized airfoil along with the previously discussed airfoils are shown in Fig. 16. The figure shows that the optimized airfoil from the constrained design has a similar aerodynamic derivatives matrix to that of the optimized airfoil from the unconstrained optimization. This results in similar frequency and damping coefficients, as shown in Fig. 17. However, while the aerodynamic derivatives matrix and flutter characteristics of the optimized airfoils for both designs are similar, the drag coefficient of the constrained optimization airfoil is about the same as the baseline airfoil. Thus, a practical airfoil of superior flutter characteristics but similar aerodynamic performance is obtained, when compared to baseline airfoil, by the proposed analysis and design method.

While no LCO-related optimization has been presented in this work, the same framework can be used for adjoint-based design driven by it. For instance, rather than maximizing flutter speed, design optimization can be carried out to minimize the amplitude of the LCO oscillations at a particular velocity by changing the objective function and the energy level of the constraint accordingly. The optimization

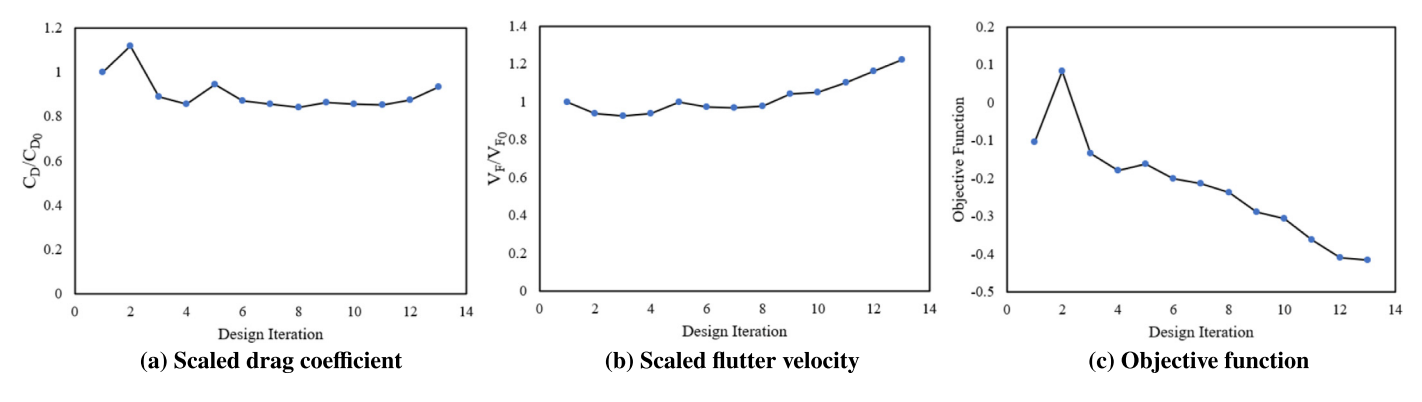


Fig. 13. Convergence history for the case with $\beta = 1.1$.

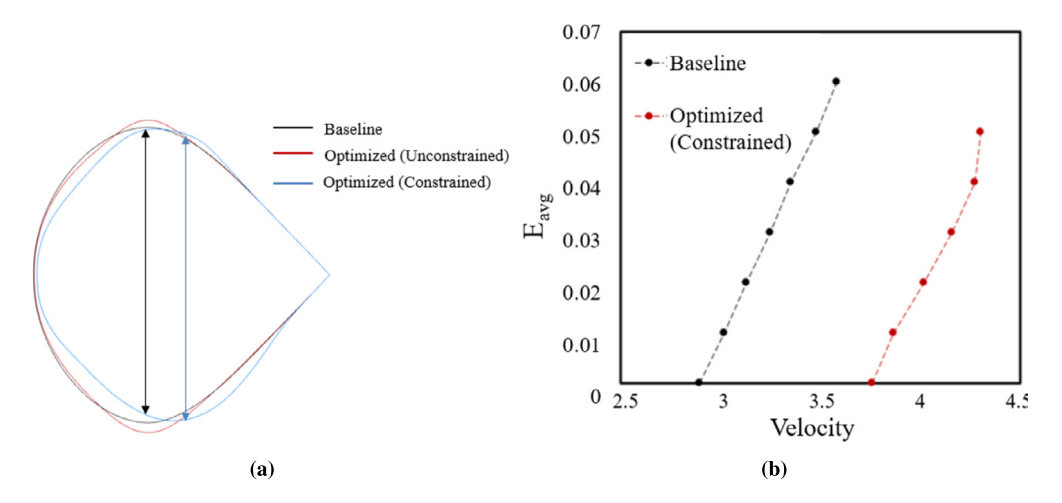


Fig. 14. (a) Comparison between baseline and optimized airfoils (b) Comparison between the LCO velocity profile for the baseline and optimized with the drag constraint.

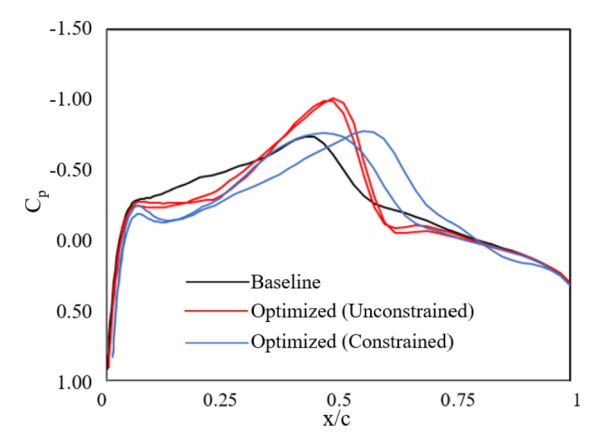


Fig. 15. Comparison of pressure coefficient distribution for the baseline and optimized airfoils (both cases).

case shown is used to showcase that the proposed framework can be used for design optimization using flutter/LCO based metrics, either as objective functions or constraints in an efficient manner.

6. Conclusion

The time-spectral method based FSI framework was developed to predict the flutter boundary and nonlinear aerodynamics based LCO conditions. A corresponding adjoint based sensitivity analysis method was also developed. The developed method was applied to a pitch-plunge airfoil section in transonic flow conditions, to predict it's flutter and LCO conditions. Results from the proposed method matched well with time accurate results. The adjoint based sensitivity analysis framework was also tested and verified for the same test case, with Hicks Henne bump functions being used as design variables and flutter velocity being the objective function.

The developed analysis and sensitivity analysis framework was then implemented in a design problem with the goal of maximizing the flutter velocity. The optimized airfoil had a greater thickness compared to the baseline airfoil. It had a high stronger shock and not only did it boast a substantially higher flutter velocity, but a higher drag as well. In order to avoid the higher drag, the objective function

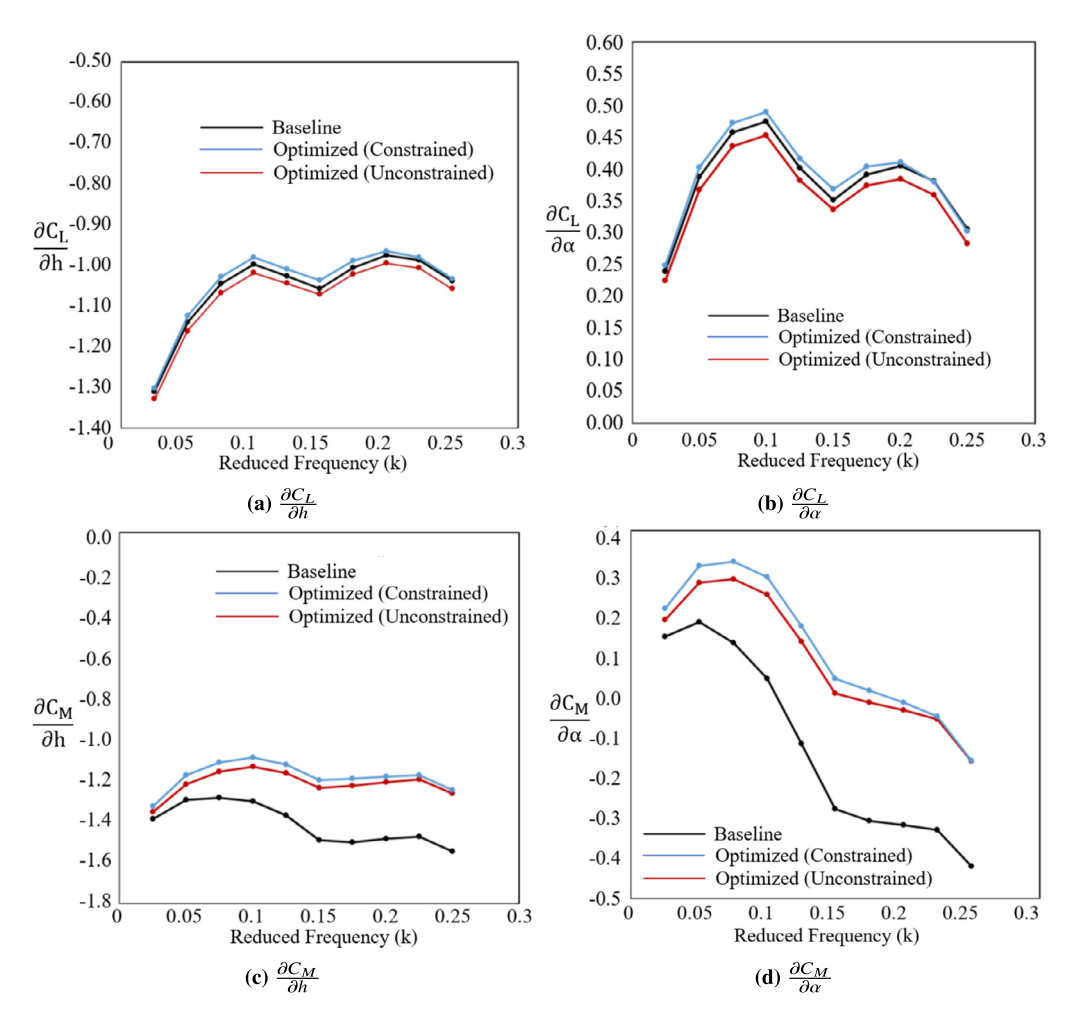


Fig. 16. Phase difference of Aerodynamic derivatives matrix coefficients for different reduced frequencies.

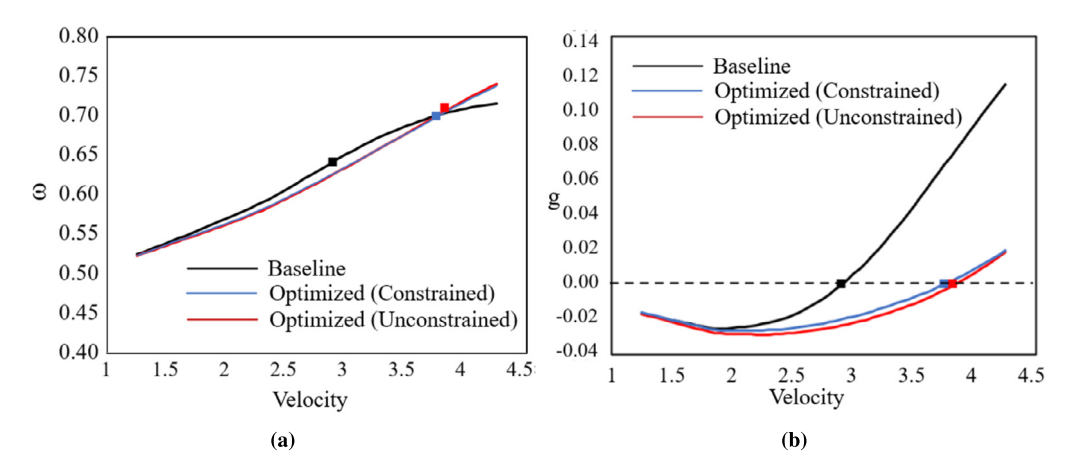


Fig. 17. Comparison of (a) Frequency and (b) Damping coefficient for the baseline and optimized airfoils (both cases).

was modified to incorporate drag coefficient as a weighted penalty term. The resulting optimized airfoil had its shock strength similar to the baseline airfoil, but its position had shifted to the aft of the airfoil. In future, this work will be extended to three dimensional wings to carry out shape optimization by modifying the entire wing surface. The flow model will also be expanded to incorporate viscous and turbulence effects.

Declaration of competing interest

The authors declare that they have no known competing financial interests or personal relationships that could have appeared to influence the work reported in this paper.

References

- [1] E.M. Lee-Rausch, J.T. Batina, Wing flutter boundary prediction using unsteady Euler aerodynamic method, J. Aircr. 32 (2) (1995) 416-422.
- [2] F. Liu, J. Cai, Y. Zhu, H.M. Tsai, A.S.F. Wong, Calculation of wing flutter by a coupled fluid-structure method, J. Aircr. 38 (2) (2001) 332–342.
- [3] C. Farhat, M. Lesoinne, P. LeTallec, Load and motion transfer algorithms for fluid/structure interaction problems with nonmatching discrete interfaces: momentum and energy conservation, optimal discretization and application to aeroelasticity, Comput. Methods Appl. Mech. Eng. 157 (1–2) (1998) 95–114.
- [4] O. Bendiksen, Transonic limit cycle flutter/LCO, in: 45th AlAA/ASME/ASCE/AHS/ASC Structures, Structural Dynamics and Materials Conference, Palm Springs, California, April 2004.
- [5] O. Bendiksen, High altitude limit cycle flutter of transonic wings, J. Aircr. 40 (1) (2002) 123–136.
- [6] L. Djayapertapa, C.B. Allen, S.P. Fiddles, Two-dimensional transonic aeroservoelastic computations in the time domain, Int. J. Numer. Methods Eng. 52 (12) (2001) 1355–1377
- [7] L. Djayapertapa, C.B. Allen, Simulation of transonic flutter and active shockwave control, Int. J. Numer. Methods Heat Fluid Flow 14 (4) (2004) 413-443.
- [8] N. Taylor, C.B. Allen, A. Gaitonde, D. Jones, C. Fenwick, G. Hill, V. Lee, Moving mesh CFD-CSD aeroservoelastic modelling of BACT wing with autonomous flap control, in: 23rd AlAA Applied Aerodynamics Conference, Totonto, Canada, Jun. 2005, AlAA Paper 2005-4840.
- [9] C.B. Allen, N.V. Taylor, C.L. Fenwick, A.L. Gaitonde, D.P. Jones, A comparison of full non-linear and reduced order aerodynamic models in control law design using a two-dimensional aerofoil model, Int. J. Numer. Methods Eng. 64 (12) (2005) 1628–1648.
- [10] K.C. Hall, J.P. Thomas, W.S. Clark, Computation of unsteady nonlinear flow in cascades using a harmonic balance technique, in: 9th International Symposium on Unsteady Aerodynamics, Aeroacoustics and Aeroelasticity of Turbomachines, Lyon, France, Sep. 2000.
- [11] K.C. Hall, J.P. Thomas, W.S. Clark, Computation of unsteady nonlinear flow in cascades using a harmonic balance technique, AIAA J. 40 (2) (2002) 879-886.
- [12] M. McMullen, A. Jameson, J.J. Alonso, Application of a nonlinear frequency domain solver to the Euler and Navier-Stokes equations, in: 40th AIAA Aerospace Sciences Meeting and Exhibit, Reno, NV, Jan. 2002, AIAA Paper 2002-120.
- [13] D. Im, S. Choi, E. Kim, J. Kwon, S. Park, Unsteady aerodynamic analysis of helicopter rotor blades using diagonal implicit harmonic balance method, J. Comput. Fluids Eng. 17 (1) (2012) 70–77.
- [14] J. Jang, S. Choi, H. Kwon, D. Im, D. Lee, J. Kwon, A preliminary study of open rotor design using a harmonic balance method, in: 50th AIAA Aerospace Sciences Meeting Including the New Horizons Forum and Aerospace Exposition, Nashville, TN, Jan. 2012.
- [15] K. Ekici, K.C. Hall, E.H. Dowell, Nonlinear analysis of unsteady flows in multistage turbomachines using harmonic balance, AIAA J. 45 (5) (2007) 1047-1057.
- [16] J. Thomas, E. Dowell, K. Hall, Nonlinear inviscid aerodynamic effects on transonic divergence, flutter, and limit-cycle oscillations, AIAA J. 40 (4) (2002) 638-646.
- [17] N. Liu, J.Q. Bai, Y. Liu, H. Jun, Efficient flutter prediction based on harmonic balance and v-g methods, Acta Aerodyn. Sin. 34 (5) (2016) 631-637.
- [18] Y. Gong, W. Zhang, Efficient aeroelastic solution based on time-spectral fluid-structure interaction method, AIAA J. (2020) 1–12.
- [19] W. Yao, S.P. Marques, Prediction of transonic LCO using an harmonic balance method, in: 44th AIAA Fluid Dynamics Conference, AIAA AVIATION Forum, 2014, AIAA 2014-2310.
- [20] A. Jameson, Aerodynamic design via control theory, J. Sci. Comput. 3 (3) (1988) 233-260.
- [21] A. Jameson, L. Martinelli, N.A. Pierce, Optimum aerodynamic design using the Navier-Stokes equations, Theor. Comput. Fluid Dyn. 10 (1-4) (1998) 213-237.
- [22] G.L.O. Halila, J.R.R.A. Martins, K.J. Fidkowski, Adjoint-based aerodynamic shape optimization including transition to turbulence effects, Aerosp. Sci. Technol. 107 (2020) 106243.
- [23] W. Chen, X. Li, W. Zhang, Suppression of vortex-induced vibration of a circular cylinder at subcritical Reynolds numbers using shape optimization, Struct. Multidiscip. Optim. 60 (5) (2019) 1–13.
- [24] W. Chen, X. Li, W. Zhang, Shape optimization to suppress the lift oscillation of flow past a stationary circular cylinder, Phys. Fluids 31 (6) (2019) 063604.
- [25] W. Xiaojing, Z. Weiwei, P. Xuhao, Z. Wang, Benchmark aerodynamic shape optimization with the POD-based CST airfoil parametric method, Aerosp. Sci. Technol. 84 (2018) 318–328.
- [26] H. Huang, K. Ekici, A discrete adjoint harmonic balance method for turbomachinery shape optimization, Aerosp. Sci. Technol. 39 (2014) 481-490.
- [27] A. Rubino, S. Vitale, P. Colonna, M. Pini, Fully-turbulent adjoint method for the unsteady shape optimization of multi-row turbomachinery, Aerosp. Sci. Technol. 106 (2020) 106132.
- [28] J.R.R.A. Martins, J.J. Alonso, J.J. Reuther, High-fidelity aerostructural design optimization of a supersonic business jet, J. Aircr. 41 (3) (2004) 523-530.
- [29] J.R.R.A. Martins, J.J. Alonso, J.J. Reuther, A coupled-adjoint sensitivity analysis method for high-fidelity aero-structural design, Optim. Eng. 6 (1) (2005) 33-62.
- [30] K. Mani, D.J. Mavriplis, Adjoint-based sensitivity formulation for fully coupled unsteady aeroelasticity problems, AIAA J. 47 (8) (2009) 1902-1915.
- [31] K. Maute, M. Nikbay, C. Farhat, Coupled analytical sensitivity analysis and optimization of three-dimensional nonlinear aeroelastic systems, AIAA J. 39 (11) (2001) 2051–2061.
- [32] J.P. Thomas, E.H. Dowell, Discrete adjoint approach for nonlinear unsteady aeroelastic design optimization, AIAA J. 57 (10) (2019) 4368-4376.
- [33] S. He, E. Jonsson, C.A. Mader, J.R.R.A. Martins, Aerodynamic shape optimization with time-spectral flutter adjoint, in: 2019 AlAA/ASCE/AHS/ASC Structures, Structural Dynamics, and Materials Conference, AlAA, San Diego, CA, January 2019.
- [34] W. Chen, C. Gao, Y. Gong, W. Zhang, Shape optimization to improve the transonic fluid-structure interaction stability by an aerodynamic unsteady adjoint method, Aerosp. Sci. Technol. 103 (2020) 105871.
- [35] A.K. Gopinath, A. Jameson, Time-spectral method for periodic unsteady computations over two- and three-dimensional bodies, in: 43rd AlAA Aerospace Sciences Meeting and Exhibit, Reno, NV, Jun. 2005, AlAA Paper 2005-1210.
- [36] T.D. Economon, F. Palacios, J.J. Alonso, Unsteady continuous adjoint approach for aerodynamic design on dynamic meshes, AIAA J. 53 (9) (2015).
- [37] R.M. Hicks, P.A. Henne, Wing design by numerical optimization, J. Aircr. 15 (7) (1978).
- [38] H. Laurent, L. Pascual, The tapenade automatic differentiation tool: principles, model and specification, ACM Trans. Math. Softw. (May 2013) 20.
- [39] G. Kalitzin, G. Medic, E. Weide, J.J. Alonso, Interaction of turbomachinery components in large scale unsteady computations of jet engines, in: 45th AIAA Aerospace Sciences Meeting and Exhibit, Reno, NV, Jan. 2007, AIAA Paper 2007-519.
- [40] S. Youcef, M.H. Schultz, GMRES: a generalized minimal residual algorithm for solving nonsymmetric linear systems, SIAM J. Sci. Stat. Comput. 7 (3) (1986) 856-869.
- [41] R. Prasad, Dynamic Aeroelastic Design Using Time-Spectral and Coupled Adjoint Method: Flutter/LCO Application, Doctoral Dissertation, Virginia Polytechnic Institute and State University, 2020.
- [42] D.C. Liu, J. Nocedal, On the limited memory BFGS method for large scale optimization, Math. Program. 45 (1989) 503-528.
- [43] S.G. Johnson, The NLopt nonlinear-optimization package, http://github.com/stevengj/nlopt.
- [44] W.H. Mason, Transonic aerodynamics of airfoils and wings, in: AOE 4124 Configuration Aerodynamics, Virginia Polytechnic Institute and State University, 2006.